bioRxiv preprint doi: https://doi.org/10.1101/2020.03.03.973131; this version posted March 31, 2020. The copyright holder for this preprint (which was not certified by peer review) is the author/funder, who has granted bioRxiv a license to display the preprint in perpetuity. It is made available under aCC-BY-NC-ND 4.0 International license.

Title: A neural code for egocentric spatial maps in the human medial temporal lobe

Authors: Lukas Kunz[1,2]*, Armin Brandt[1], Peter C. Reinacher[3,4], Bernhard P. Staresina[5,6], Eric T. Reifenstein[7], Christoph T. Weidemann[2,8], Nora A. Herweg[9], Melina Tsitsiklis[10], Richard Kempter[7], Michael J. Kahana[9], Andreas Schulze-Bonhage[1#], Joshua Jacobs[2#]

Affiliations:

[1]Epilepsy Center, Medical Center – University of Freiburg, Faculty of Medicine, University of Freiburg, Freiburg im Breisgau, Germany.

[2]Department of Biomedical Engineering, Columbia University, New York, NY, USA.

[3]Department of Stereotactic and Functional Neurosurgery, Medical Center – University of Freiburg, Faculty of Medicine, University of Freiburg, Freiburg im Breisgau, Germany.

[4]Fraunhofer Institute for Laser Technology, Aachen, Germany.

[5]School of Psychology, University of Birmingham, Birmingham B15 2TT, UK.

[6]Centre for Human Brain Health, University of Birmingham, Birmingham B15 2TT, UK.

[7]Institute for Theoretical Biology, Department of Biology, Humboldt-Universität zu Berlin, Berlin, Germany.

[8]Department of Psychology, Swansea University, Swansea SA2 8PP, UK.

[9]Computational Memory Lab, Department of Psychology, University of Pennsylvania, Philadelphia, PA, USA.

[10]Doctoral Program in Neurobiology and Behavior, Columbia University, New York, NY, USA.

[#]These authors contributed equally to this work.

*Correspondence to: lukas.kunz@uniklinik-freiburg.de.

bioRxiv preprint doi: https://doi.org/10.1101/2020.03.03.973131; this version posted March 31, 2020. The copyright holder for this preprint (which was not certified by peer review) is the author/funder, who has granted bioRxiv a license to display the preprint in perpetuity. It is made available under aCC-BY-NC-ND 4.0 International license.

Abstract:

Spatial navigation relies on neural systems that encode spatial information relative to the external world or relative to the navigating organism. Ever since the proposal of cognitive maps, the neuroscience of spatial navigation has focused on allocentric (world-referenced) representations such as place cells. Here, using single-neuron recordings during virtual navigation, we reveal a neural code for egocentric (self-centered) spatial information in humans: "anchor cells" represent egocentric directions towards proximal "anchor points" located in the environmental center or periphery. Anchor cells were abundant in parahippocampal cortex, supported full vectorial representations of egocentric space, and were integrated into a neural memory network. Anchor cells may thus facilitate egocentric navigation strategies, assist in transforming percepts into allocentric spatial representations, and may underlie the first-person perspective in episodic memories.

One Sentence Summary:

Anchor cells in the human brain provide the neural basis for a self-centered coordinate system during spatial navigation.

bioRxiv preprint doi: https://doi.org/10.1101/2020.03.03.973131; this version posted March 31, 2020. The copyright holder for this preprint (which was not certified by peer review) is the author/funder, who has granted bioRxiv a license to display the preprint in perpetuity. It is made available under aCC-BY-NC-ND 4.0 International license.

Main text:

Detailed neural representations of space form the neurobiological basis of successful navigation and accurate spatial memory. Traditionally, the neuroscience of spatial navigation has focused on allocentric representations, which encode spatial information in coordinates relative to the external world: a place cell may indicate if an animal or human is in the "northeast" corner of an environment (*1*, *2*), a head-direction cell may activate whenever navigating "south" (*3*), and a boundary vector/border cell may respond to a spatial boundary located to the "west" (*4*, *5*). However, spatial environments are primarily experienced from a first-person, egocentric perspective—requiring neural codes that provide spatial information in relation to the self. Via transformation circuits (*6*, *7*), egocentric representations (*8–10*) may then be converted into their allocentric counterparts (*4*, *5*, *11*) for abstract knowledge and long-term storage (*12*).

Despite abundant behavioral evidence that humans employ egocentric spatial information to accomplish wayfinding (*12*, *13*), little is known about the neural basis of egocentric spatial representations in humans. Here, we hypothesized that neurons in human medial temporal lobe (MTL) keep track of the instantaneous relationship between the navigating subject and proximal areas of the environment. Specifically, we targeted the identification of "anchor cells" whose activity encodes the subject's egocentric direction towards local reference points ("anchor points"). Such a coding scheme would be instrumental for egocentric navigation, because it provides orientation in relation to the proximal spatial layout and allows route planning from a first-person perspective.

To detect and characterize human anchor cells, we recorded single-neuron activity from the MTL of 14 neurosurgical epilepsy patients (table S1), while they performed an object–location memory task in a virtual environment (Fig. 1, A and B). In this task (*14*), patients learned and repeatedly retrieved the locations of eight different objects. While patients freely navigated the virtual environment throughout the task, their virtual heading directions and locations were recorded to associate these variables with single-neuron activity. Patients contributed a total of 18 sessions (duration between 22 and 74 min) and completed between 34 and 167 trials per session. Patients performed the task well, as spatial memory performance was above chance on 83% of the trials (Fig. 1C) and performance increased over the course of the session (Wilcoxon test, z=2.896, P=0.004; Fig. 1D). Across all sessions, we recorded a total of N=729 neurons from amygdala (n=242), entorhinal cortex (n=114), fusiform gyrus (n=25), hippocampus (n=146), parahippocampal cortex (n=65), temporal pole (n=128) and visual cortex (n=9; figs. S1 and S2).

We identified anchor cells by analyzing each neuron's firing rate as a function of the patient's egocentric direction ("bearing") towards local reference points in the virtual environment [Fig. 1E; figs. S3 and S4; supplementary text; (*15*)]. Briefly, for each cell we iterated through 112 "candidate anchor points" (Fig. 1F), each time assessing the degree to which the cell's firing rate varied as a function of the subject's egocentric bearing towards this candidate anchor point. The center of mass of the largest cluster of significant candidate anchor points ("anchor field") defined the anchor point (Fig. 1G). This analysis procedure thus resulted in

bioRxiv preprint doi: https://doi.org/10.1101/2020.03.03.973131; this version posted March 31, 2020. The copyright holder for this preprint (which was not certified by peer review) is the author/funder, who has granted bioRxiv a license to display the preprint in perpetuity. It is made available under aCC-BY-NC-ND 4.0 International license.

the identification of individual neurons that behaved as anchor cells by tracking the subject's bearing towards their anchor points within the virtual environment.

We observed 95 anchor cells, 13.0% of all neurons, which is significantly more than expected by chance (binomial test versus 5% chance, $P<0.001$). On average, there were 5.3 ± 1.3 (mean ± SEM) anchor cells per session. At least one anchor cell was found in 16 of 18 sessions and in twelve of 14 patients. Anchor cells exhibited anchor points in various locations of the environment and showed a range of preferred egocentric bearings towards these anchor points (Fig. 2). For example, the anchor cell in Fig. 2A had its anchor point in the "northeast" part of the environment (Fig. 2A, left), and the cell's firing rate increased when this anchor point was ~45° to the right of the subject's current heading (Fig. 2A, middle). We illustrate this cell's tuning towards its anchor point by plotting the cell's preferred allocentric direction as a function of location (Fig. 2A, right). For anchor cells, this "vector-field map" often exhibited a systematic change in the cell's preferred allocentric direction across the environment. Such a pattern is fundamentally different from the homogeneous vector-field maps of neurons encoding allocentric direction (see below).

Anchor cells were most prevalent in parahippocampal cortex (30.8%; Fig. 3A), which is the human homologue of the rodent postrhinal cortex (*16*). Some anchor cells showed additional firing-rate modulations related to the patients' allocentric direction or location (Fig. 3B; fig. S5), but a significant number of "pure" anchor cells remained after excluding anchor cells that were also direction and/or place cells ($n=60$; 8.2%; binomial test, $P<0.001$). Across cells, anchor points were positioned in many different locations of the environment, including both the center and the periphery (Hartigan's dip test, $P<0.001$; Fig. 3, C and D). The anchor cells with anchor points in the center of the environment are potentially related to the previously identified "center-bearing cells" (*16*) and "path cells" (*17*). The preferred bearings of anchor cells with anchor points in the center of the environment showed a bimodal distribution with an overrepresentation of "ahead" and "behind" bearings (Rayleigh test for two-fold symmetry, $z=13.619$, $P<0.001$; Fig. 3E), whereas anchor cells with anchor points in the periphery showed a roughly uniform distribution of preferred anchor bearings (Fig. 3F).

To reveal whether anchor cells support a full vectorial representation of egocentric space, we next tested for anchor cells that represented the distance towards the anchor point, in addition to bearing. Hence, for time periods when the subject's current anchor bearing was in alignment (±90°) with the cell's preferred anchor bearing, we examined whether the cell's activity represented the subject's anchor-point distance. Indeed, 23 of 95 anchor cells showed positive or negative firing-rate changes according to the patient's distance to the anchor point (13 and 10, respectively; binomial tests, both $P<0.028$; Fig. 3, G and H), comparable to the prevalence of distance tuning found in other spatial cell types (*9*, *16*). This kind of full vectorial representation of space in egocentric coordinates could be useful for navigation by allowing the navigating organism not only to estimate the direction, but also to compute the location of the anchor point relative to itself.

Beyond navigation, do anchor cells have a role in spatial memory? To answer this question, we examined (i) their overlap with "memory-sensitive cells"; (ii) variations in their tuning strengths associated with spatial memory performance; and (iii) their relationship to "object

bioRxiv preprint doi: https://doi.org/10.1101/2020.03.03.973131; this version posted March 31, 2020. The copyright holder for this preprint (which was not certified by peer review) is the author/funder, who has granted bioRxiv a license to display the preprint in perpetuity. It is made available under aCC-BY-NC-ND 4.0 International license.

cells". First, we examined the overlap between anchor cells and memory-sensitive cells, which changed their firing in relation to the patients' spatial memory performance. We found many memory-sensitive cells in various MTL regions (Fig. 3I), including neurons that increased (n=59; binomial test, P<0.001; Fig. 3J) or decreased (n=69; binomial test, P<0.001; Fig. 3K) their firing rates in association with good memory performance. The finding of both positive and negative memory-sensitive cells is in line with previous human single-neuron recordings (*18*), and negative memory-sensitive cells may relate to inhibitory engrams, which are negative replicas of excitatory memory representations (*19*). We observed that anchor cells were strongly integrated into the memory network, as memory-related firing rate changes were common among anchor cells (29 of 95 anchor cells fulfilled the criteria for being memory-sensitive cells; 30.5%; chi-squared test, χ^2=12.691, P<0.001). In comparison, characteristics of memory-sensitive neurons were not particularly common among direction or place cells (23.8% and 21.1%, respectively; both χ^2<2.563, both P>0.109; Fig. 3L).

Second, to understand whether anchor-cell properties varied with spatial memory performance, we examined the relationship between performance and the precision of the anchor cells' directional tuning. We observed that a subset of anchor cells showed more precise anchor-cell tuning (i.e., higher Rayleigh vector lengths of the tuning curve) during task periods when subjects showed better spatial memory performance (11 of 95; binomial test, P=0.008; e.g., Fig. 3, M and N). This phenomenon was more common among anchor cells that had preferred anchor bearings pointing "ahead" as compared to those with preferred anchor bearings pointing "behind" (chi-squared test, χ^2=4.117, P=0.042). Sharper tuning of anchor cells with anchor points ahead of the navigating organism may thus contribute to successful spatial navigation and accurate spatial memory.

In a third step, we examined the relationship between anchor and object cells (n=118; binomial test, P<0.001; fig. S6), which provided neural representations of the objects whose locations had to be learned and retrieved throughout the task. For example, an object cell increased its activity during trials in which the patient had to remember and re-encode the location of the globe (fig. S6A). A significant number of anchor cells fulfilled the criteria for being an object cell (27 of 95; binomial test, P<0.001; chi-squared test, χ^2=12.052, P<0.001). These conjunctive anchor–object cells may constitute a neural interface between spatial and non-spatial task features, which could be instrumental in reinstating the egocentric spatial context upon a non-spatial cue during memory recall.

Theoretical accounts of spatial navigation and memory suggest that neural transformation circuits combine egocentric spatial representations with allocentric direction information in order to create allocentric spatial representations such as place cells (*6*, *7*). Thus, after demonstrating anchor cells that represent spatial information in egocentric coordinates, we tested for single-neuron codes of allocentric direction. We identified 76 "direction cells", which showed increased firing when patients were heading towards specific global directions (binomial test, P<0.001). For example, direction cells activated when the subject was moving "west" (Fig. 4, A and B). As expected, direction cells exhibited more consistent directional tuning across the environment than anchor cells (i.e., more homogeneous vector-field maps; Wilcoxon test, z=5.392, P<0.001; Fig. 4, C and D), illustrating the difference in their coding

bioRxiv preprint doi: https://doi.org/10.1101/2020.03.03.973131; this version posted March 31, 2020. The copyright holder for this preprint (which was not certified by peer review) is the author/funder, who has granted bioRxiv a license to display the preprint in perpetuity. It is made available under aCC-BY-NC-ND 4.0 International license.

schemes (supplementary text). Direction cells were particularly present in parahippocampal cortex and hippocampus (Fig. 4E). Across the population, their preferred directions were broadly distributed, but showed a bias towards a large mountain in the environment's background (binomial test, P=0.004; Fig. 4, F and G). This bias of preferred directions towards a prominent distal landmark resembles findings in rodents (*20*) and provides neural evidence for the importance of visual cues in human spatial navigation (*21*), which may stabilize the transformation circuits (*7*). Converging projections from anchor and direction cells may then lead to allocentric spatial representations in downstream neurons.

Our results demonstrate anchor cells as a neural code for egocentric spatial information in the human brain. Such a code provides the subject with orientation relative to the proximal spatial layout, allows route planning from a first-person perspective, and may assist in imagining future scenarios from an egocentric viewpoint. Anchor cells may thus constitute a neural substrate of egocentric navigation strategies in human spatial behavior (*12*, *13*). Anchor cells were most prevalent in parahippocampal cortex, suggesting a cellular explanation for the detrimental effects of parahippocampal lesions on navigation and memory tasks that require egocentric reference frames (*22*, *23*). The abundance of anchor cells in parahippocampal cortex may furthermore explain neural responses of the "parahippocampal place area" to spatial scenes (*24*, *25*), because the presentation of spatial scenes from a first-person perspective may activate the anchor-cell network.

Anchor-cell functioning may constitute an essential component in the processing hierarchy of the brain's navigation and memory system: During navigation, anchor cells may extract egocentric spatial information from sensory input. Then, by transforming anchor-cell activity into world-referenced coordinates, allocentric spatial representations may emerge in order to enable long-term storage and semantic, self-independent knowledge (*26*). Specifically, the transformation of anchor-cell activity into allocentric coordinates may directly lead to neural activity as seen in spatial view cells (*27*), spatial target cells (*18*), or place cells that represent remote locations (*28–30*). During memory retrieval, allocentric spatial representations may be transformed back into anchor-cell responses that reinstate the original, egocentrically experienced, spatial context of the memory (*7*). Anchor cells may thus play a role beyond spatial navigation by providing a neural substrate of the first-person perspective during the retrieval of spatial and episodic memories.

bioRxiv preprint doi: https://doi.org/10.1101/2020.03.03.973131; this version posted March 31, 2020. The copyright holder for this preprint (which was not certified by peer review) is the author/funder, who has granted bioRxiv a license to display the preprint in perpetuity. It is made available under aCC-BY-NC-ND 4.0 International license.

References and Notes:

1. J. O'Keefe, J. Dostrovsky, The hippocampus as a spatial map. Preliminary evidence from unit activity in the freely-moving rat. *Brain Res.* **34**, 171–175 (1971).
2. A. D. Ekstrom *et al.*, Cellular networks underlying human spatial navigation. *Nature*. **425**, 184–188 (2003).
3. J. S. Taube, R. U. Muller, J. B. Ranck, Head-direction cells recorded from the postsubiculum in freely moving rats. I. Description and quantitative analysis. *J. Neurosci.* **10**, 420–35 (1990).
4. T. Solstad, C. N. Boccara, E. Kropff, M.-B. Moser, E. I. Moser, Representation of geometric borders in the entorhinal cortex. *Science*. **322**, 1865–8 (2008).
5. C. Lever, S. Burton, A. Jeewajee, J. O'Keefe, N. Burgess, Boundary vector cells in the subiculum of the hippocampal formation. *J. Neurosci.* **29**, 9771–7 (2009).
6. C. Wang, X. Chen, J. J. Knierim, Egocentric and allocentric representations of space in the rodent brain. *Curr. Opin. Neurobiol.* **60**, 12–20 (2020).
7. A. Bicanski, N. Burgess, A neural-level model of spatial memory and imagery. *Elife*. **7** (2018), doi:10.7554/eLife.33752.
8. A. Sarel, A. Finkelstein, L. Las, N. Ulanovsky, Vectorial representation of spatial goals in the hippocampus of bats. *Science*. **355**, 176–180 (2017).
9. C. Wang *et al.*, Egocentric coding of external items in the lateral entorhinal cortex. *Science*. **362**, 945–949 (2018).
10. J. R. Hinman, G. W. Chapman, M. E. Hasselmo, Neuronal representation of environmental boundaries in egocentric coordinates. *Nat. Commun.* **10**, 2772 (2019).
11. Ø. A. Høydal, E. R. Skytøen, S. O. Andersson, M.-B. Moser, E. I. Moser, Object-vector coding in the medial entorhinal cortex. *Nature*. **568**, 400–404 (2019).
12. N. Burgess, Spatial memory: how egocentric and allocentric combine. *Trends Cogn. Sci.* **10**, 551–557 (2006).
13. A. D. Ekstrom, E. A. Isham, Human spatial navigation: representations across dimensions and scales. *Curr. Opin. Behav. Sci.* **17**, 84–89 (2017).
14. L. Kunz *et al.*, Reduced grid-cell-like representations in adults at genetic risk for Alzheimer's disease. *Science*. **350**, 430–3 (2015).
15. Materials and methods are available as supplementary materials.
16. P. A. LaChance, T. P. Todd, J. S. Taube, A sense of space in postrhinal cortex. *Science*. **365**, eaax4192 (2019).
17. J. Jacobs, M. J. Kahana, A. D. Ekstrom, M. V Mollison, I. Fried, A sense of direction in human entorhinal cortex. *Proc. Natl. Acad. Sci. U. S. A.* **107**, 6487–92 (2010).
18. M. Tsitsiklis *et al.*, Single-Neuron Representations of Spatial Targets in Humans. *Curr. Biol.* **30**, 245-253.e4 (2020).
19. H. C. Barron, T. P. Vogels, T. E. Behrens, M. Ramaswami, Inhibitory engrams in perception and memory. *Proc. Natl. Acad. Sci. U. S. A.* **114** (2017), pp. 6666–6674.
20. L. Acharya, Z. M. Aghajan, C. Vuong, J. J. Moore, M. R. Mehta, Causal Influence of Visual Cues on Hippocampal Directional Selectivity. *Cell*. **164**, 197–207 (2016).
21. A. D. Ekstrom, Why vision is important to how we navigate. *Hippocampus*. **25**, 731–735 (2015).
22. G. Weniger, E. Irle, Posterior parahippocampal gyrus lesions in the human impair egocentric learning in a virtual environment. *Eur. J. Neurosci.* **24**, 2406–2414 (2006).
23. C. J. Ploner *et al.*, Lesions Affecting the Parahippocampal Cortex Yield Spatial Memory Deficits in Humans. *Cereb. Cortex*. **10**, 1211–1216 (2000).
24. R. Epstein, N. Kanwisher, A cortical representation of the local visual environment. *Nature*. **392**, 598–601 (1998).

bioRxiv preprint doi: https://doi.org/10.1101/2020.03.03.973131; this version posted March 31, 2020. The copyright holder for this preprint (which was not certified by peer review) is the author/funder, who has granted bioRxiv a license to display the preprint in perpetuity. It is made available under aCC-BY-NC-ND 4.0 International license.

25. F. Mormann *et al.*, Scene-selective coding by single neurons in the human parahippocampal cortex. *Proc. Natl. Acad. Sci. U. S. A.* **114**, 1153–1158 (2017).
26. G. Buzsáki, E. I. Moser, Memory, navigation and theta rhythm in the hippocampal-entorhinal system. *Nat. Neurosci.* **16**, 130–138 (2013).
27. E. T. Rolls, Spatial view cells and the representation of place in the primate hippocampus. *Hippocampus*. **9** (1999), pp. 467–480.
28. B. E. Pfeiffer, D. J. Foster, Hippocampal place-cell sequences depict future paths to remembered goals. *Nature*. **497**, 74–79 (2013).
29. P. E. Jercog *et al.*, Heading direction with respect to a reference point modulates place-cell activity. *Nat. Commun.* **10**, 2333 (2019).
30. M. Shahi *et al.*, Hippocampal anchor fields. *Soc. Neurosci. Annu. Meet.* (2019).
31. I. Fried *et al.*, Cerebral microdialysis combined with single-neuron and electroencephalographic recording in neurosurgical patients. *J. Neurosurg.* **91**, 697–705 (1999).
32. F. J. Chaure, H. G. Rey, R. Quian Quiroga, A novel and fully automatic spike-sorting implementation with variable number of features. *J. Neurophysiol.* **120**, 1859–1871 (2018).
33. E. F. Kutter, J. Bostroem, C. E. Elger, F. Mormann, A. Nieder, Single Neurons in the Human Brain Encode Numbers. *Neuron*. **100**, 753-761.e4 (2018).
34. T. P. Reber *et al.*, Representation of abstract semantic knowledge in populations of human single neurons in the medial temporal lobe. *PLOS Biol.* **17**, e3000290 (2019).
35. L. Kunz *et al.*, Hippocampal theta phases organize the reactivation of large-scale electrophysiological representations during goal-directed navigation. *Sci. Adv.* **5**, eaav8192 (2019).
36. C. F. Doeller, J. A. King, N. Burgess, Parallel striatal and hippocampal systems for landmarks and boundaries in spatial memory. *Proc. Natl. Acad. Sci. U. S. A.* **105**, 5915–20 (2008).
37. D. Chen *et al.*, Hexadirectional Modulation of Theta Power in Human Entorhinal Cortex during Spatial Navigation. *Curr. Biol.* **28**, 3310-3315.e4 (2018).
38. C. F. Doeller, C. Barry, N. Burgess, Evidence for grid cells in a human memory network. *Nature*. **463**, 657–661 (2010).
39. J. Miller *et al.*, Lateralized hippocampal oscillations underlie distinct aspects of human spatial memory and navigation. *Nat. Commun.* **9**, 2423 (2018).
40. S. E. Qasim *et al.*, Memory retrieval modulates spatial tuning of single neurons in the human entorhinal cortex. *Nat. Neurosci.*, 433862 (2019).
41. E. R. Wood, P. A. Dudchenko, R. J. Robitsek, H. Eichenbaum, Hippocampal Neurons Encode Information about Different Types of Memory Episodes Occurring in the Same Location. *Neuron*. **27**, 623–633 (2000).
42. J. R. Manns, M. W. Howard, H. Eichenbaum, Gradual Changes in Hippocampal Activity Support Remembering the Order of Events. *Neuron*. **56**, 530–540 (2007).
43. N. Burgess, F. Cacucci, C. Lever, J. O'Keefe, Characterizing multiple independent behavioral correlates of cell firing in freely moving animals. *Hippocampus*. **15**, 149–153 (2005).
44. K. Hardcastle, N. Maheswaranathan, S. Ganguli, L. M. Giocomo, A Multiplexed, Heterogeneous, and Adaptive Code for Navigation in Medial Entorhinal Cortex. *Neuron*. **94** (2017), doi:10.1016/j.neuron.2017.03.025.
45. R. Oostenveld, P. Fries, E. Maris, J.-M. Schoffelen, FieldTrip: Open source software for advanced analysis of MEG, EEG, and invasive electrophysiological data. *Comput. Intell. Neurosci.* **2011**, 156869 (2011).
46. P. Berens, CircStat: A MATLAB Toolbox for Circular Statistics. *J. Stat. Softw.* **31**, 1–

bioRxiv preprint doi: https://doi.org/10.1101/2020.03.03.973131; this version posted March 31, 2020. The copyright holder for this preprint (which was not certified by peer review) is the author/funder, who has granted bioRxiv a license to display the preprint in perpetuity. It is made available under aCC-BY-NC-ND 4.0 International license.

21 (2009).

47. J. A. Hartigan, P. M. Hartigan, The Dip Test of Unimodality. *Ann. Stat.* **13**, 70–84 (1985).

48. J. F. Miller *et al.*, Neural activity in human hippocampal formation reveals the spatial context of retrieved memories. *Science*. **342**, 1111–4 (2013).

49. G. Chen, J. A. King, Y. Lu, F. Cacucci, N. Burgess, Spatial cell firing during virtual navigation of open arenas by head-restrained mice. *Elife*. **7** (2018), doi:10.7554/eLife.34789.

50. T. Shuman *et al.*, Breakdown of spatial coding and interneuron synchronization in epileptic mice. *Nat. Neurosci.* **23**, 229–238 (2020).

51. M. C. M. Faraut *et al.*, Dataset of human medial temporal lobe single neuron activity during declarative memory encoding and recognition. *Sci. Data*. **5**, 180010 (2018).

bioRxiv preprint doi: https://doi.org/10.1101/2020.03.03.973131; this version posted March 31, 2020. The copyright holder for this preprint (which was not certified by peer review) is the author/funder, who has granted bioRxiv a license to display the preprint in perpetuity. It is made available under aCC-BY-NC-ND 4.0 International license.

Acknowledgements:

We are grateful for all the patients who volunteered to participate in this study. We thank the clinical team of the Freiburg Epilepsy Center for their continuous support, D. Lachner-Piza for technical assistance, and S. Qasim, M. Peer, and D. Schonhaut for comments on the manuscript.

Funding:

L.K., A.B., E.T.R., R.K., and A.S.-B. were supported by the Federal Ministry of Education and Research (BMBF; 01GQ1705A). L.K., A.B., M.T., A.S.-B., and J.J. received funding via National Science Foundation (NSF) grant BCS-1724243. L.K., A.B., and A.S.-B. were supported by National Institutes of Health (NIH) grant 563386 and NIH/NINDS grant U01 NS1113198-01. L.K. was supported by a travel grant from the Boehringer Ingelheim Fonds (Mainz, Germany). P.C.R. received research grants from the Fraunhofer Society (Munich, Germany) and from the Else Kröner-Fresenius Foundation (Bad Homburg, Germany) and personal fees, travel support, and honoraria for lectures from Boston Scientific (Marlborough, MA, USA), Brainlab (Munich, Germany) and Inomed (Emmendingen, Germany). N.A.H. received funding via the German Research Foundation (DFG; HE 8302/1-1). B.P.S. was supported by a Wellcome Trust/Royal Society Sir Henry Dale Fellowship (107672/Z/15/Z). M.T. and J.J. were supported by NIH grant MH104606. M.J.K. was supported by NIH grants MH55687 and MH061975.

Author contributions:

L.K. and J.J. designed the study; L.K., A.B., P.C.R, and A.S.-B. recruited participants; P.C.R. implanted electrodes; L.K. and A.B. collected data; L.K. performed analyses with contributions from B.P.S., E.T.R., C.T.W., N.A.H., M.T., and R.K.; A.S.-B., J.J., M.J.K., and R.K. acquired the necessary resources and financial support as well as managed and supervised the project; L.K. and J.J. wrote the paper; all authors reviewed and edited the final manuscript.

Competing interests:

Authors declare no competing interests.

Data and materials availability:

All data and software used to analyze the data are available upon request from the corresponding author. Code and data will be made publicly available after publication.

bioRxiv preprint doi: https://doi.org/10.1101/2020.03.03.973131; this version posted March 31, 2020. The copyright holder for this preprint (which was not certified by peer review) is the author/funder, who has granted bioRxiv a license to display the preprint in perpetuity. It is made available under aCC-BY-NC-ND 4.0 International license.

List of Supplementary Materials:

Materials and Methods

Supplementary Text

Figures S1-S6

Table S1

References (*31-51*)

bioRxiv preprint doi: https://doi.org/10.1101/2020.03.03.973131; this version posted March 31, 2020. The copyright holder for this preprint (which was not certified by peer review) is the author/funder, who has granted bioRxiv a license to display the preprint in perpetuity. It is made available under aCC-BY-NC-ND 4.0 International license.

Figures:

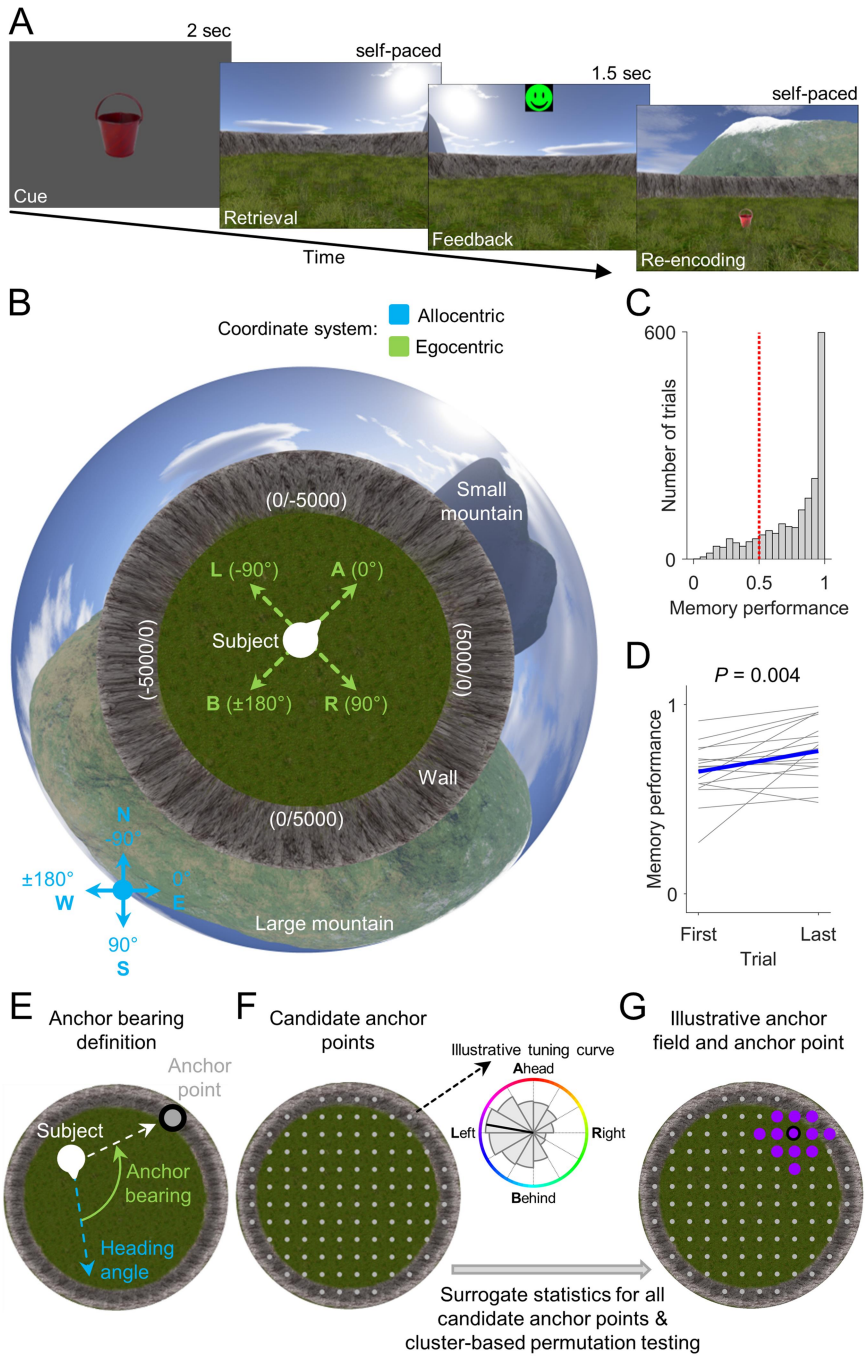

Fig. 1. Task, performance, and illustration of anchor-cell identification. (**A**) Patients performed an object–location memory task in a virtual environment. In each trial, a given object had to be placed at its correct location. Patients received feedback depending on response accuracy and re-encoded the object location afterwards. (**B**) Bird's eye view of the environment. Blue compass, allocentric direction; green compass, egocentric direction (given the patient is facing "northeast"). A (B; L; R), ahead (behind; to the left; to the right). (**C**) Histogram of spatial memory performance values across all trials. Red line, chance level. (**D**) Change in spatial memory performance between the first and the last trial. Blue line, mean

bioRxiv preprint doi: https://doi.org/10.1101/2020.03.03.973131; this version posted March 31, 2020. The copyright holder for this preprint (which was not certified by peer review) is the author/funder, who has granted bioRxiv a license to display the preprint in perpetuity. It is made available under aCC-BY-NC-ND 4.0 International license.

across subjects. (**E**) Illustration of anchor bearing, which is the difference between the allocentric heading angle and the angle of the vector from the subject's location to the anchor point. (**F**) Left, candidate anchor points. Right, illustrative tuning curve for one candidate point depicting firing rate as a function of bearing towards this point. Significance of each point is tested via surrogate statistics. (**G**) Cluster-based permutation testing identifies the largest cluster of significant candidate points ("anchor field"). The "anchor point" is the center of mass of the anchor field.

bioRxiv preprint doi: https://doi.org/10.1101/2020.03.03.973131; this version posted March 31, 2020. The copyright holder for this preprint (which was not certified by peer review) is the author/funder, who has granted bioRxiv a license to display the preprint in perpetuity. It is made available under aCC-BY-NC-ND 4.0 International license.

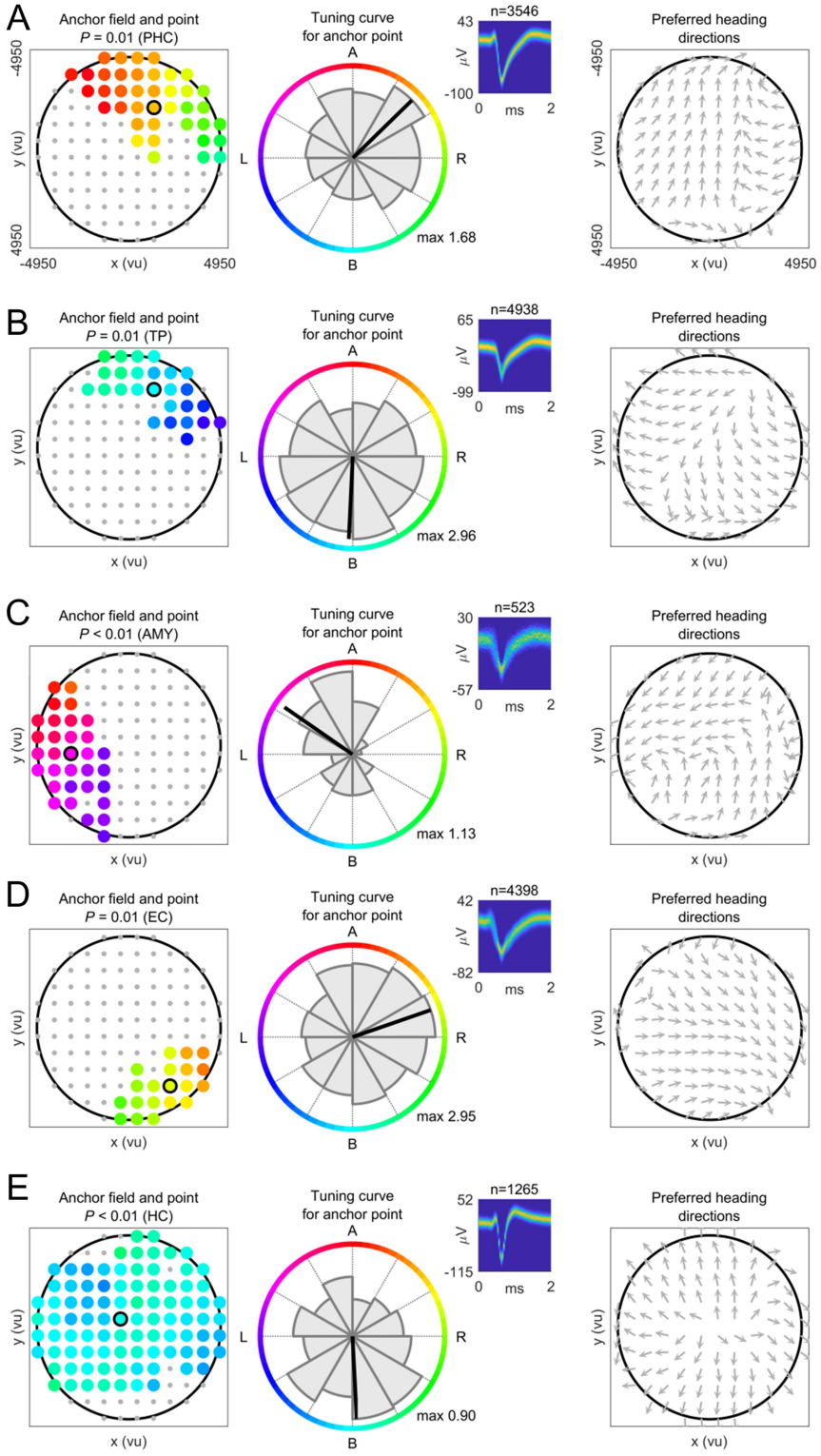

Fig. 2. Anchor cells activate as a function of egocentric bearing towards anchor points. (**A-E**) Examples of anchor cells. Left column, anchor-cell plot showing the anchor field (colored dots) and the anchor point (colored dot with black circle). Coloring depicts the preferred egocentric bearing towards each location of the anchor field. The color code corresponds to the colored circle in the middle column. For example, a green-colored dot indicates that the cell activates when this location is to the right of the subject. Gray dots,

bioRxiv preprint doi: https://doi.org/10.1101/2020.03.03.973131; this version posted March 31, 2020. The copyright holder for this preprint (which was not certified by peer review) is the author/funder, who has granted bioRxiv a license to display the preprint in perpetuity. It is made available under aCC-BY-NC-ND 4.0 International license.

non-significant candidate anchor points. Large black circle, environmental boundary. *P*-value, significance from cluster-based permutation testing. Middle column, tuning curve showing how the cell's firing rate varies as a function of egocentric bearing towards the anchor point; max, maximum firing rate (Hz). Colored circle indicates bearing. Inset depicts spike-density plot (number above inset indicates spike number entering the analysis). Right column, vector-field map showing the cell's preferred allocentric heading direction across the environment (gray arrows). Black circle, environmental boundary. A (B; L; R), anchor point ahead (behind; to the left; to the right). ms, milliseconds; vu, virtual units. AMY, amygdala; EC, entorhinal cortex; HC, hippocampus; PHC, parahippocampal cortex; TP, temporal pole.

bioRxiv preprint doi: https://doi.org/10.1101/2020.03.03.973131; this version posted March 31, 2020. The copyright holder for this preprint (which was not certified by peer review) is the author/funder, who has granted bioRxiv a license to display the preprint in perpetuity. It is made available under aCC-BY-NC-ND 4.0 International license.

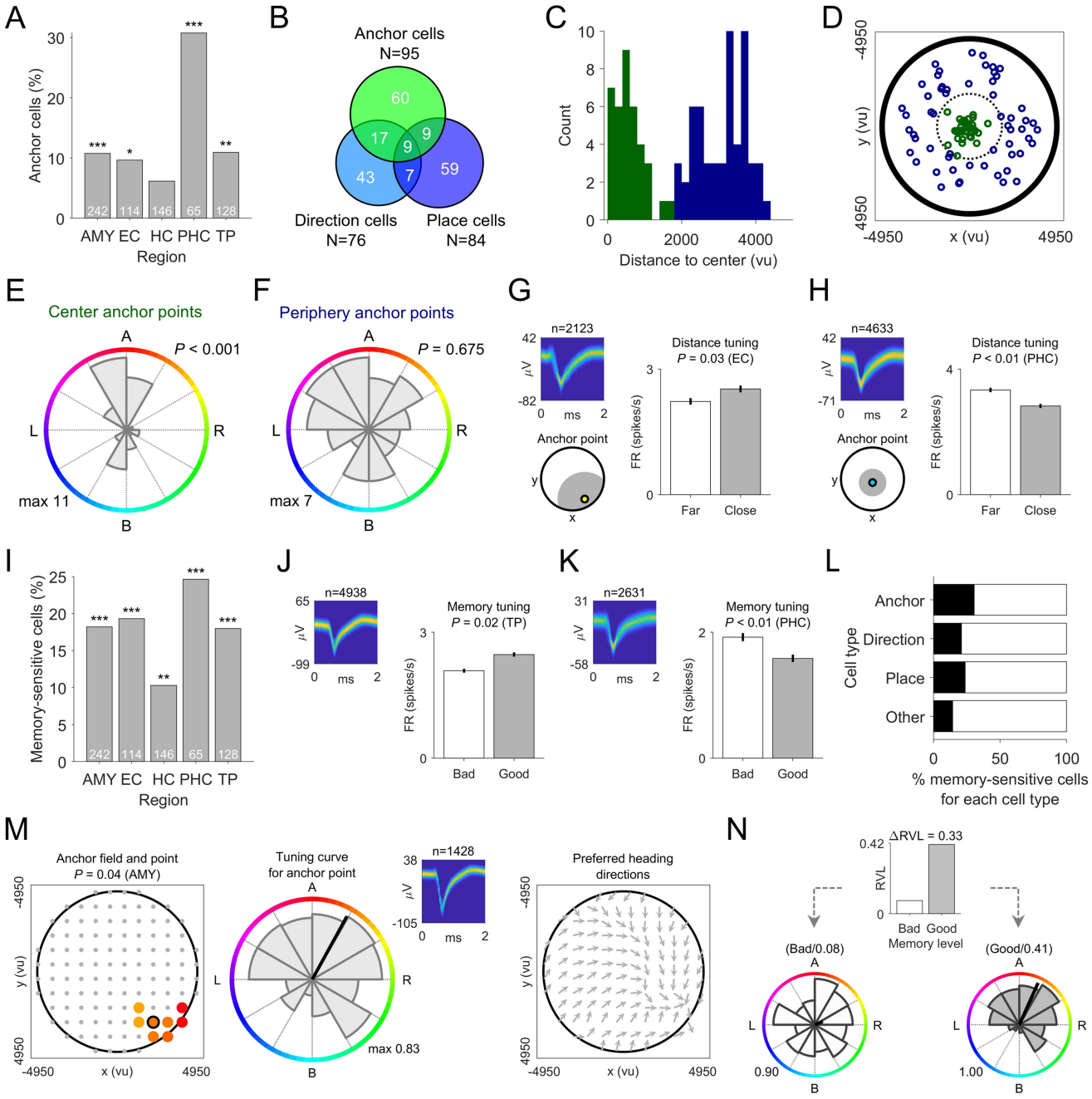

Fig. 3. Anchor cells have anchor points in various locations, exhibit distance tuning, and show memory modulation. (**A**) Distribution of anchor cells across brain regions. (**B**) Overlap between anchor, direction, and place cells. (**C**) Distribution of anchor-point distances to the environmental center. Green, center anchor points; blue, periphery anchor points. (**D**) Anchor-point locations. Black dotted line separates center anchor points (green) from periphery anchor points (blue). (**E-F**) Distribution of preferred bearings towards anchor points in the environmental center (**E**) or periphery (**F**). (**G-H**) Example anchor cells showing activity correlated with anchor-point distance. Bottom left subpanel indicates the anchor point, with close (gray) and far (white) locations. (**I**) Distribution of memory-sensitive cells across regions. (**J-K**) Examples of memory-sensitive cells increasing (**J**) or decreasing (**K**) their firing rate in relation to good versus bad memory performance. (**L**) Overlap between

bioRxiv preprint doi: https://doi.org/10.1101/2020.03.03.973131; this version posted March 31, 2020. The copyright holder for this preprint (which was not certified by peer review) is the author/funder, who has granted bioRxiv a license to display the preprint in perpetuity. It is made available under aCC-BY-NC-ND 4.0 International license.

memory-sensitive cells and anchor cells. (**M-N**) Example anchor cell (**M**) exhibiting more precise tuning during periods with better memory performance (**N**). A (B; L; R), anchor point ahead (behind; to the left; to the right). AMY, amygdala; EC, entorhinal cortex; HC, hippocampus; PHC, parahippocampal cortex; TP, temporal pole. max, maximum number; ms, milliseconds; RVL, Rayleigh vector length; vu, virtual units. **P*<0.05; ***P*<0.01; ****P*<0.001.

bioRxiv preprint doi: https://doi.org/10.1101/2020.03.03.973131; this version posted March 31, 2020. The copyright holder for this preprint (which was not certified by peer review) is the author/funder, who has granted bioRxiv a license to display the preprint in perpetuity. It is made available under aCC-BY-NC-ND 4.0 International license.

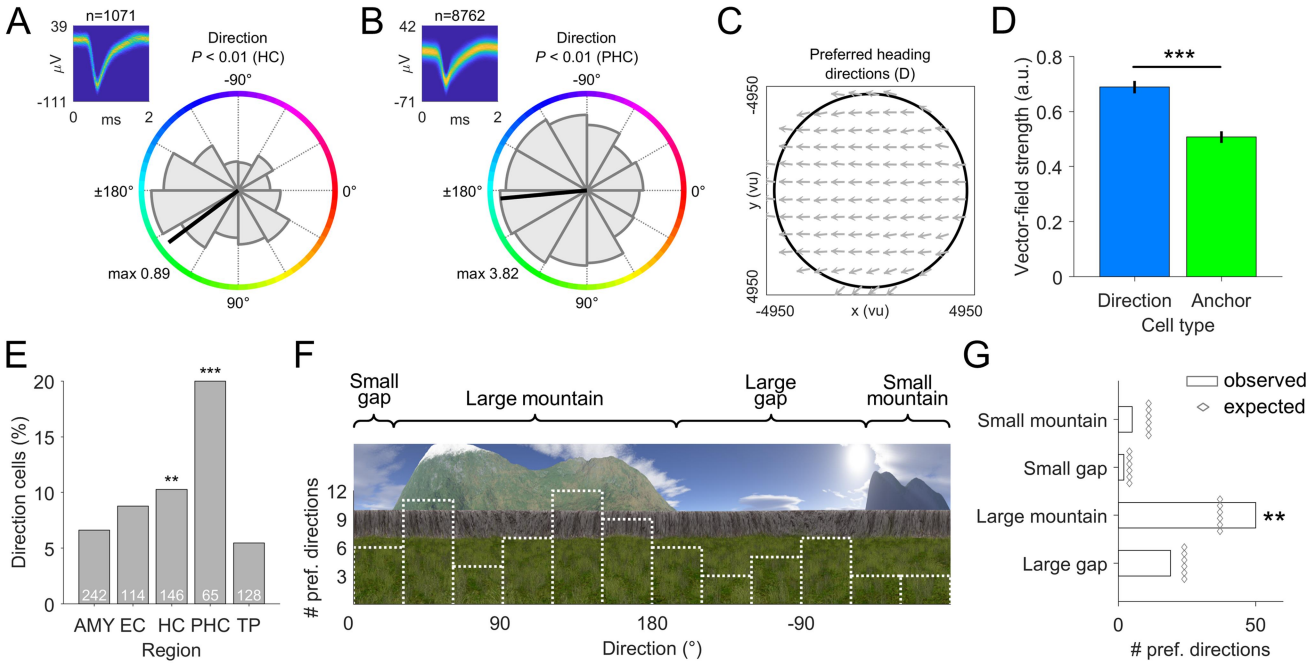

Fig. 4. Direction cells represent allocentric direction. (**A-B**) Examples of direction cells encoding allocentric direction. Gray shaded area, tuning curve; black line, preferred direction; colored circle, allocentric direction; max, maximum firing rate (Hz). Upper left subpanels show spike-density plots (number above subpanel indicates spike count). (**C**) Example vector-field map of the direction cell shown in (**B**), illustrating that allocentric direction tuning is similar across the environment. (**D**) Comparison of vector-field strengths between direction cells and anchor cells. (**E**) Distribution of direction cells across brain regions. (**F**) Distribution of preferred directions of allocentric direction cells (white dotted line), shown relative to the background scenery in the virtual environment. (**G**) Bar graph showing the number of preferred directions tuned towards different distal landmarks of the environment's background. White bars, observed number of preferred directions oriented towards a specific distal landmark; gray diamonds, number of preferred directions expected by chance. AMY, amygdala; EC, entorhinal cortex; HC, hippocampus; PHC, parahippocampal cortex; TP, temporal pole. a.u., arbitrary units; ms, milliseconds; pref., preferred; vu, virtual units. ***P*<0.01; ****P*<0.001.

bioRxiv preprint doi: https://doi.org/10.1101/2020.03.03.973131; this version posted March 31, 2020. The copyright holder for this preprint (which was not certified by peer review) is the author/funder, who has granted bioRxiv a license to display the preprint in perpetuity. It is made available under aCC-BY-NC-ND 4.0 International license.

Supplementary Materials

Materials and Methods

Experimental model and subject details

14 human subjects (seven female; age range, 19-51 years; mean age ± SEM, 33.1 ± 3.0 years) undergoing treatment for pharmacologically intractable epilepsy participated in the study. Informed written consent was obtained from all patients. The study conformed to the guidelines of the ethics committee of the University Hospital Freiburg, Freiburg im Breisgau, Germany.

Neurophysiological recordings

Patients were surgically implanted with intracranial depth electrodes in the MTL for diagnostic purposes in order to isolate the epileptic seizure focus for potential subsequent surgical resection. The exact electrode numbers and locations varied across subjects and were determined solely by clinical needs. Neuronal signals were recorded using Behnke-Fried depth electrodes (Ad-Tech Medical Instrument Corp., Racine, WI). Each depth electrode contained a bundle of nine platinum-iridium microelectrodes with a diameter of 40 µm that protruded from the tip of the depth electrode (*31*). The first eight microelectrodes were used to record action potentials and local field potentials. The ninth microelectrode served as reference. Microelectrode coverage included amygdala, entorhinal cortex, fusiform gyrus, hippocampus, parahippocampal cortex, temporal pole, and visual cortex. We recorded microwire data at 30 kHz using NeuroPort (Blackrock Microsystems, Salt Lake City, UT).

Spike detection and sorting

Neuronal spikes were detected and sorted using Wave_Clus (*32*). We used default settings with the following exceptions: “template_sdnum” was set to 1.5 to assign unsorted spikes to clusters in a more conservative manner; “min_clus” was set to 60 and “max_clus” was set to 10 in order to avoid over-clustering; and “mintemp” was set to 0.05 to avoid under-clustering. All clusters were visually inspected and judged based on the spike shape and its variance, inter-spike interval (ISI) distribution, and the presence of a plausible refractory period [following (*33*)]. If necessary, clusters were manually adjusted or excluded. Furthermore, clusters were excluded that exhibited mean firing rates of <0.1 Hz during the analysis time window [following (*2*)]. Spike waveforms are shown as spike-density plots in all figures [following (*34*)].

In total, we identified N=729 clusters (also referred to as “neurons” or “cells” throughout the manuscript) across 18 experimental sessions from all 14 patients. Because different sessions from the same patient were separated by >12 h, we treated neuronal responses of these

bioRxiv preprint doi: https://doi.org/10.1101/2020.03.03.973131; this version posted March 31, 2020. The copyright holder for this preprint (which was not certified by peer review) is the author/funder, who has granted bioRxiv a license to display the preprint in perpetuity. It is made available under aCC-BY-NC-ND 4.0 International license.

sessions as statistically independent units. An experienced rater (B.P.S.) assigned the tips of depth electrodes to brain regions based on post-implantation MRI scans in native space so that neurons recorded from the corresponding microelectrodes could be assigned to these regions. We recorded n=242 neurons from amygdala, n=114 neurons from entorhinal cortex, n=25 neurons from fusiform gyrus, n=146 neurons from hippocampus, n=65 neurons from parahippocampal cortex, n=128 neurons from temporal pole, and n=9 from visual cortex. Due to low numbers of neurons in fusiform gyrus and visual cortex, we excluded these regions from region-specific analyses.

For recording quality assessment (fig. S2), we calculated the number of units recorded on each wire; the ISI refractoriness for each unit; the mean firing rate for each unit; and the waveform peak signal-to-noise ratio (SNR) for each unit. The ISI refractoriness was assessed as the percentage of ISIs with a duration of <3 ms. The waveform peak SNR was determined as: $SNR=A_{peak}/STD_{noise}$, where A_{peak} is the absolute amplitude of the peak of the mean waveform, and STD_{noise} is the standard deviation of the raw data trace (filtered between 300 and 3,000 Hz).

Task

During experimental sessions, patients sat in bed and performed an object–location memory task on a laptop computer (Fig. 1), which was adapted from previous studies (*14*, *35–38*).

During the task, patients first learned the locations of eight everyday objects by collecting each object from its location once (this initial learning phase was excluded from all analyses). Afterwards, patients completed variable numbers of test trials (Fig. 1A) depending on compliance. Each test trial started with an inter-trial-interval of 3-5 s duration (uniformly distributed). Patients were then presented with one of the eight objects (“cue”; duration of 2 s). During the subsequent retrieval period (“retrieval”; self-paced), patients navigated to the assumed object location and indicated their arrival via a button press. Next, patients received feedback on the accuracy of their response using one of five different emoticons (“feedback”; duration of 1.5 s). Response accuracy was measured as the Euclidean distance between the response location and the correct location (“drop error”). The retrieved object then appeared in its correct location and patients collected it from there in order to further improve their associative object-location memories (“re-encoding”; self-paced).

Drop errors were transformed into spatial memory performance values by ranking each drop error within 1 million potential drop errors. Potential drop errors were the distances between the trial-specific correct object location and random locations within the virtual environment. This transformation accounted for the fact that the possible range of drop errors is smaller for object locations in the center of the virtual environment as compared to object locations in the periphery of the virtual environment (*39*). A spatial memory performance value of 1 represents the smallest possible drop error, whereas a spatial memory performance value of 0 represents the largest possible drop error.

The virtual environment comprised a grassy plain [diameter of 10,000 virtual units (vu)] surrounded by a cylindrical cliff. There were no landmarks within the environment. The

bioRxiv preprint doi: https://doi.org/10.1101/2020.03.03.973131; this version posted March 31, 2020. The copyright holder for this preprint (which was not certified by peer review) is the author/funder, who has granted bioRxiv a license to display the preprint in perpetuity. It is made available under aCC-BY-NC-ND 4.0 International license.

background scenery comprised a large and a small mountain, clouds, and the sun (Fig. 1, A and B). All distal landmarks were rendered at infinity and remained stationary throughout the task.

Patients navigated the virtual environment using the arrow keys of the laptop computer (forward, turn left, turn right). Instantaneous virtual locations and heading directions (which are identical with viewing directions in our task) were sampled at 50 Hz. We aligned the behavioral data with the electrophysiological data via visual triggers, which were detected by a phototransistor attached to the screen of the laptop computer. The phototransistor signal was recorded together with the electrophysiological data at a temporal resolution of 30 kHz.

General statistical procedure

At each time point (sampled at 50 Hz), the participant's allocentric direction and location was given by the yaw value and the (x/y)-coordinate of the virtual character's position in the virtual environment, respectively. Neuronal spike times were adjusted to the behavioral time axis according to the trigger time stamps. We then down-sampled the behavioral data to 10 Hz [following (*17*)] and calculated the neuronal firing rate (spikes/s) for each time bin. Time periods in which the patient remained stationary for >2 s were excluded from the analysis.

To identify different cell types, we employed an ANOVA framework (*2*, *18*, *40–42*), in which we assessed the effects of different factors on firing rates. To identify direction and place cells, we used a two-way ANOVA with factors "direction" and "place". To identify anchor cells, we used a three-way ANOVA with factors "direction", "place", and "anchor bearing". To identify object cells, we used a three-way ANOVA with factors "direction", "place", and "object". In all ANOVAs (computed via MATLAB's *anovan* function), we used Type II sums of squares, which controls for main effects of other factors when determining significance of a given factor. Empirical *F*-values of a given factor were considered significant, when they exceeded the 95th percentile of 101 surrogate *F*-values which we obtained by performing the same ANOVA on circularly shifted firing rates [with the end of the session wrapped to the beginning; following, e.g., (*40*)].

Tuning curves are displayed as the estimated marginal means of a given factor when controlling for the other factors (computed via MATLAB's *multcompare* function), inspired by analysis procedures in rodents that identify independent effects of different factors on firing rates (*43*, *44*).

All analyses were carried out in MATLAB 2018b using MATLAB toolboxes and custom MATLAB scripts. Unless otherwise indicated, we considered results statistically significant when the corresponding *P*-value fell below an alpha-level of α=0.05. Analyses were two-sided, if not otherwise notified. Binomial tests evaluated the significance of proportions of neurons relative to a chance level of 5% (two-sided), if not otherwise specified. Surrogate statistics were generally one-sided to assess whether an empirical test statistic exceeded a distribution of surrogate statistics significantly (*45*). Statistics on angular data were carried out using the CircStat toolbox (*46*). The significance of overlaps between different cell types was assessed using chi-squared tests.

bioRxiv preprint doi: https://doi.org/10.1101/2020.03.03.973131; this version posted March 31, 2020. The copyright holder for this preprint (which was not certified by peer review) is the author/funder, who has granted bioRxiv a license to display the preprint in perpetuity. It is made available under aCC-BY-NC-ND 4.0 International license.

Anchor cells

We identified anchor cells using a two-step procedure (Fig. 1, F and G). In the first step, separately for each candidate anchor point, we analyzed each neuron's firing rate via a three-way ANOVA with factors "direction", "place", and "anchor bearing" to assess the relevance of "anchor bearing" while controlling for "direction" and "place". We calculated anchor bearings as the angular difference between the subject's instantaneous heading angle and the concurrent angle of the vector from the subject's location to the anchor point (Fig. 1E). Candidate anchor points (n=112) were evenly distributed across the virtual environment (distance between neighboring candidate anchor points, 900 vu; Fig. 1F). No candidate anchor points were located outside the circular boundary. The factors "direction" and "anchor bearing" could take on one of twelve values (angular resolution, 30°). The factor "place" could take on one of 100 values representing a 10 x 10 grid overlaid onto the virtual environment (bin edge length, 900 vu). Only factor levels with ≥5 separate observations (for example, five temporally distinct visits to location bin i) were included to ensure sufficient behavioral sampling. For the factor "anchor bearing" we then extracted the raw ANOVA F-value ($F_{\text{empirical}}$) and the corresponding estimated firing rate map ($\text{eFR}_{\text{empirical}}$), which is the tuning curve of the firing rate as a function of "anchor bearing" while controlling for "direction" and "place" (for examples, see the middle column of Fig. 2). Using the circular-shift procedure described above, we estimated surrogate F-values ($F_{\text{surrogate}}$) and surrogate estimated firing rate maps ($\text{eFR}_{\text{surrogate}}$). A candidate anchor point was considered significant, if its $F_{\text{empirical}}$ value exceeded the 95$^{\text{th}}$ percentile of its $F_{\text{surrogate}}$ values (corresponding to P<0.05).

In the second step, we employed cluster-based permutation testing (*45*) to assess the overall significance of the cell regarding anchor-bearing tuning: contiguous clusters of significant candidate anchor points were identified and their percentiles of $F_{\text{empirical}}$ within $F_{\text{surrogate}}$ were summed up, resulting in a $\text{cluster-percentile}_{\text{empirical}}$ value (for example, a contiguous cluster of 10 significant candidate anchor points, where all candidate anchor points had a percentile value of 97%, resulted in a cluster-percentile value of 970%). We considered this $\text{cluster-percentile}_{\text{empirical}}$ value statistically significant, if it exceeded the 95$^{\text{th}}$ percentile of surrogate $\text{cluster-percentile}_{\text{surrogate}}$ values (corresponding to P<0.05). Here, $\text{cluster-percentile}_{\text{surrogate}}$ values were created by using each of the $F_{\text{surrogate}}$ matrices as a hypothetical empirical matrix once, each time assessing its $\text{cluster-percentile}_{\text{surrogate}}$ value by comparing it against all other matrices (both the remaining $F_{\text{surrogate}}$ matrices and the $F_{\text{empirical}}$ matrix), as described above.

For each anchor cell, we show the contiguous cluster of significant candidate anchor points (i.e., the "anchor field"; e.g., Fig. 2A, left): each significant candidate anchor point is depicted as a colored, bold dot; non-significant candidate anchor points are indicated as gray, small dots. Coloring corresponds to the circular mean of the estimated firing rate map $\text{eFR}_{\text{empirical}}$ for that candidate anchor point (for example, red means that the neuron's firing rate increased when the subject was moving towards this point; cyan means that the neuron's firing rate increased when the subject was moving away from this point). We obtained each cell's "anchor point" by calculating the center of mass of the anchor field using MATLAB's

bioRxiv preprint doi: https://doi.org/10.1101/2020.03.03.973131; this version posted March 31, 2020. The copyright holder for this preprint (which was not certified by peer review) is the author/funder, who has granted bioRxiv a license to display the preprint in perpetuity. It is made available under aCC-BY-NC-ND 4.0 International license.

regionprops function. We note that the terms "anchor field" and "anchor point" have been used before to describe the tuning of hippocampal place cells towards reference points (*30*).

Vector-field maps

As an approximate illustration of the cell's anchor-bearing tuning, we additionally show the cell's preferred allocentric direction as a function of location (e.g., Fig. 2A, right). Here, the location-specific allocentric direction tuning curve is estimated via a two-way ANOVA with factors "direction" and "place", which takes only data points into account when the subject is in the vicinity of the corresponding candidate anchor point [the vicinity of a candidate anchor point is defined as the point's (x/y)-coordinate ± 3,333 vu]. For example, the vector-field map in Fig. 2A, right, shows that allocentric direction tuning of this cell varies across different locations, twisting towards a spot in the northeast part of the virtual environment. This vector-field map can thus illustrate the anchor-cell plot. Of note, the vector-field map does not match the anchor-cell plot closely in cases when direction and anchor bearing explain relevant and independent amounts of variance in the firing rates. This is due to the fact that the anchor-cell plot shows anchor-bearing tuning while accounting for the effects of direction and location (three-way ANOVA with factors "direction", "place", and "anchor bearing"), whereas the vector-field map shows direction tuning while only accounting for the effect of location (two-way ANOVA with factors "direction" and "place").

Preferred bearing of anchor cells

For each anchor cell, we extracted its preferred bearing towards the anchor point via the circular mean of the corresponding tuning curve. Bimodality of preferred anchor bearings was tested by applying a Rayleigh test on the preferred anchor bearings multiplied by two.

Spatial organization of anchor points

We evaluated bimodality of anchor-point distances towards the environmental center using Hartigan's dip test (*47*) and separated the two groups using MATLAB's *kmeans* function.

Distance tuning of anchor cells

To investigate whether anchor cells encoded the distance towards the anchor point, we analyzed each anchor cell's firing rate as a function of Euclidean distance towards the anchor point. Only time points, when the subject's current anchor bearing was in alignment with the cell's preferred anchor bearing (±90°) were considered for this analysis. We then tested whether firing rates significantly increased or decreased when the subject was "far" from or "close" to the anchor point (median split of distance values). To this end, we performed a two-sample *t*-test between firing rates associated with far versus close distances from the anchor point and extracted the resulting *t*-statistic ($t_{empirical}$) for each anchor cell. To obtain surrogate *t*-statistics ($t_{surrogate}$), we circularly shifted the empirical firing rates 401 times in relation to the behavioral data. We considered a cell to exhibit distance tuning, if $t_{empirical}$ exceeded the 95th percentile of $t_{surrogate}$ values (positive distance tuning) or if it fell below the 5th percentile of $t_{surrogate}$ values (negative distance tuning).

bioRxiv preprint doi: https://doi.org/10.1101/2020.03.03.973131; this version posted March 31, 2020. The copyright holder for this preprint (which was not certified by peer review) is the author/funder, who has granted bioRxiv a license to display the preprint in perpetuity. It is made available under aCC-BY-NC-ND 4.0 International license.

Anchor-cell tuning and memory performance

To establish a relationship between the specificity of the tuning curve of anchor cells and spatial memory performance, we divided the data into two data parts based on a median split of spatial memory performance values (resulting in two memory levels: "good" and "bad"). For each data part, we used the three-way ANOVA with factors "direction", "place", and "anchor bearing" towards the anchor point (identified using the entire data) to extract the estimated firing rate map $eFR_{empirical\text{-}part}$ for the factor "anchor bearing". We estimated the precision of $eFR_{empirical\text{-}part}$ as the Rayleigh vector length (RVL), separately for each data part (RVL_{part}), and calculated the difference between data part-specific RVLs as: $\Delta RVL = diff(RVL_{part})$. For each anchor cell, we then tested whether its ΔRVL value was above the 95th percentile of 401 surrogate ΔRVL values obtained by performing the analysis on circularly shifted firing rates. We tested whether the proportion of these memory-modulated anchor cells were more common among anchor cells with preferred anchor bearings pointing "ahead" (i.e., "ahead" ± 90°) as compared to anchor cells with preferred anchor bearings pointing "behind" (i.e., "behind" ± 90°) using a chi-squared test.

Direction cells and place cells

Rodent head-direction cells (*3*) activate whenever an animal's head is pointing in a specific global direction that is defined relative to a world-referenced coordinate system (for example, when the head is pointing "north" or "south"). Here, we identified "direction cells" that exhibited firing-rate modulations as a function of the patients' current heading direction within the virtual environment.

To identify direction cells, we analyzed each neuron's activity by means of a two-way ANOVA with factors "direction" and "place". The factor "direction" could take on one of twelve values (angular resolution, 30°). The factor "place" could take on one of 100 values representing a 10 x 10 grid overlaid onto the virtual environment (bin edge length, 900 vu). Only factor levels with ≥5 separate observations were included to ensure sufficient behavioral sampling. We then extracted the raw ANOVA *F*-value for the factor "direction" ($F_{empirical}$) and the estimated firing rate map ($eFR_{empirical}$), while controlling for the factor "place". We calculated statistical significance of $F_{empirical}$ values using surrogate statistics as described above. For each direction cell, we extracted its preferred direction via the circular mean of the directional tuning curve.

To test whether preferred directions were biased towards the distal landmarks, we divided the background scenery into the following parts: large mountain, large gap, small mountain, and small gap. For each landmark we then counted how often a preferred direction pointed towards it ($N_{observed}$). We tested for significance of landmark-specific $N_{observed}$ values using binomial tests against chance levels, which were separately estimated for each landmark based on its angular extension.

To compare the vector-field maps of direction cells with the vector-field maps of anchor cells, we computed "vector-field strengths" as the Rayleigh vector length of all vectors in the vector-field map (a completely homogeneous vector-field map would result in a Rayleigh

bioRxiv preprint doi: https://doi.org/10.1101/2020.03.03.973131; this version posted March 31, 2020. The copyright holder for this preprint (which was not certified by peer review) is the author/funder, who has granted bioRxiv a license to display the preprint in perpetuity. It is made available under aCC-BY-NC-ND 4.0 International license.

vector length of 1.0; a completely inhomogeneous vector-field map would result in a Rayleigh vector length of 0.0).

We identified place cells via the same procedure as described for direction cells using a two-way ANOVA with factors "direction" and "place". We defined place bins as those spatial bins in which the empirical firing rate exceeded the 95th percentile of surrogate firing rates [following (*2*)].

Memory-sensitive cells

We identified memory-sensitive cells as those cells exhibiting significantly increased or decreased firing rates during periods with good versus bad spatial memory performance (median split of spatial memory performance values). To this end, we performed a two-sample *t*-test for each cell between firing rates associated with good versus bad spatial memory performance and extracted the resulting *t*-statistic ($t_{empirical}$). Surrogate statistics were obtained as described above. We labeled a neuron as "memory-sensitive", if $t_{empirical}$ exceeded the 95th percentile of $t_{surrogate}$ values (positive memory-sensitive cell) or if it fell below the 5th percentile of $t_{surrogate}$ values (negative memory-sensitive cell).

Object cells

To identify object cells, we analyzed each neuron's activity using a three-way ANOVA with factors "direction", "place", and "object". The factor "object" could take on one of eight different values (because each patient learned and retrieved the locations of eight different objects). For all time bins of a given trial, the factor "object" had the same value. We obtained object cells and preferred objects [i.e., objects for which the cell's empirical firing rate exceeded the 95th percentile of surrogate firing rates (*2*)] using surrogate statistics as described above. Cells without a preferred object were excluded from the object-cell population.

To examine whether the preferred objects of object cells with ≥2 preferred objects exhibited a specific spatial relationship, we estimated the average Euclidean distance between the locations of all preferred objects, separately for each object cell with ≥2 preferred objects, and averaged across cells afterwards ($D_{empirical}$). We created 401 surrogate values ($D_{surrogate}$) for comparison by randomly selecting *n* object locations per cell, where *n* corresponds to the number of preferred objects of a given cell. We then determined the percentile of $D_{empirical}$ within $D_{surrogate}$ to test whether $D_{empirical}$ was smaller than the 5th percentile of $D_{surrogate}$-values (in this case, locations of preferred objects would be closer to each other as expected by chance).

bioRxiv preprint doi: https://doi.org/10.1101/2020.03.03.973131; this version posted March 31, 2020. The copyright holder for this preprint (which was not certified by peer review) is the author/funder, who has granted bioRxiv a license to display the preprint in perpetuity. It is made available under aCC-BY-NC-ND 4.0 International license.

Supplementary Text

Tuning strengths of spatially modulated neurons

Tuning strengths of spatially modulated cells in our study were generally lower than in rodents. For example, head-direction cells in rodents often exhibit baseline firing rates of about 0 spikes/s and increase their firing rates up to about 100 spikes/s at the preferred head direction (*3*). Directionally sensitive neurons in our study showed only moderate firing rate increases when subjects moved in the preferred direction [for similar tuning strengths, see, e.g., (*2*, *18*, *40*, *48*)]. Thus, the use of the classical terminology (e.g., the term "place cells" to refer to spatially modulated neurons) should be treated with caution (we adhere to these terms for ease of reading).

Different factors may contribute to this reduced selectivity of neuronal responses: In humans, it is not possible to adjust the localization of microelectrodes after implantation and a search for strongly tuned cells is thus not possible. Moreover, patients did not physically navigate the spatial environment, but rather completed a virtual navigation task, potentially associated with broader spatial tuning (*49*). Additionally, neuronal firing in the human brain may be higher-dimensional than in rodents meaning that more internal and external factors (including ongoing thoughts, spontaneous occurrence of memories and ideas, and stimuli in the patient's room) influence neuronal firing rates. Finally, (subtle) epileptogenic processes may have also affected the sharpness of the neurons' tuning curves (*50*). Reassuringly, control analyses showed a significant proportion of anchor cells after excluding neurons from the anchor-cell analysis that were recorded on microelectrodes located in brain regions potentially involved in the generation of epileptic seizures as defined by clinical criteria (80 anchor cells of 570 cells; 14.0%; binomial test, $P<0.001$).

Relationship between anchor cells and direction cells

Anchor cells encode egocentric direction towards local reference points, whereas direction cells encode allocentric direction. However, egocentric direction towards a reference point becomes increasingly similar to allocentric direction with increasing distance of the reference point from the subject.

In the main text, we showed that the homogeneity of vector-field maps differed between anchor cells and direction cells. We performed additional analyses to clarify the relationship between anchor cells and direction cells. First, to provide evidence that anchor-cell tuning did not spuriously arise due to potential collinearities between the factors "direction" and "anchor bearing" in our three-way ANOVA framework designed to identify anchor cells, we performed this ANOVA on surrogate data instead of empirical data [testing for significance of the tuning curves by comparing against other surrogate data; following (*33*)]. In this way, we empirically estimated the percentage of anchor cells that may have arisen due to chance (for example, due to interdependencies between the factors "direction" and "anchor bearing"). As expected, this approach resulted in $n=34$ (4.7%) statistically significant outcomes (i.e., false positives), confirming the *a priori* chosen alpha level of $\alpha=0.05$.

bioRxiv preprint doi: https://doi.org/10.1101/2020.03.03.973131; this version posted March 31, 2020. The copyright holder for this preprint (which was not certified by peer review) is the author/funder, who has granted bioRxiv a license to display the preprint in perpetuity. It is made available under aCC-BY-NC-ND 4.0 International license.

Second, we performed the anchor-cell analysis using a two-way ANOVA, with factors "place" and "anchor bearing", in order to test for the number of anchor cells when not controlling for allocentric direction in our ANOVA framework. Using this approach, we observed n=110 anchor cells (15.1%; binomial test, P<0.001; as reported in the main text, we identified 95 anchor cells when also controlling for allocentric direction). Furthermore, anchor cell test statistics (i.e., each cell's cluster-percentile$_{empirical}$ value) were highly similar between both types of ANOVA (Spearman correlation, ρ_{727}=0.626, P<0.001) and the overlap between anchor cells identified via the two different analyses was significantly higher than expected by chance (chi-squared test, χ^2=148.630, P<0.001).

In sum, these analyses show (i) that anchor cells exhibit essential differences in their tuning as compared to direction cells; (ii) that anchor cells do not spuriously arise from potential collinearities between the factors "direction" and "anchor bearing" in our ANOVA framework; and (iii) that anchor cells can also be identified in an ANOVA framework with a reduced number of predictors (i.e., with factors "place" and "anchor bearing" instead of "direction", "place", and "anchor bearing").

bioRxiv preprint doi: https://doi.org/10.1101/2020.03.03.973131; this version posted March 31, 2020. The copyright holder for this preprint (which was not certified by peer review) is the author/funder, who has granted bioRxiv a license to display the preprint in perpetuity. It is made available under aCC-BY-NC-ND 4.0 International license.

Supplementary Figures

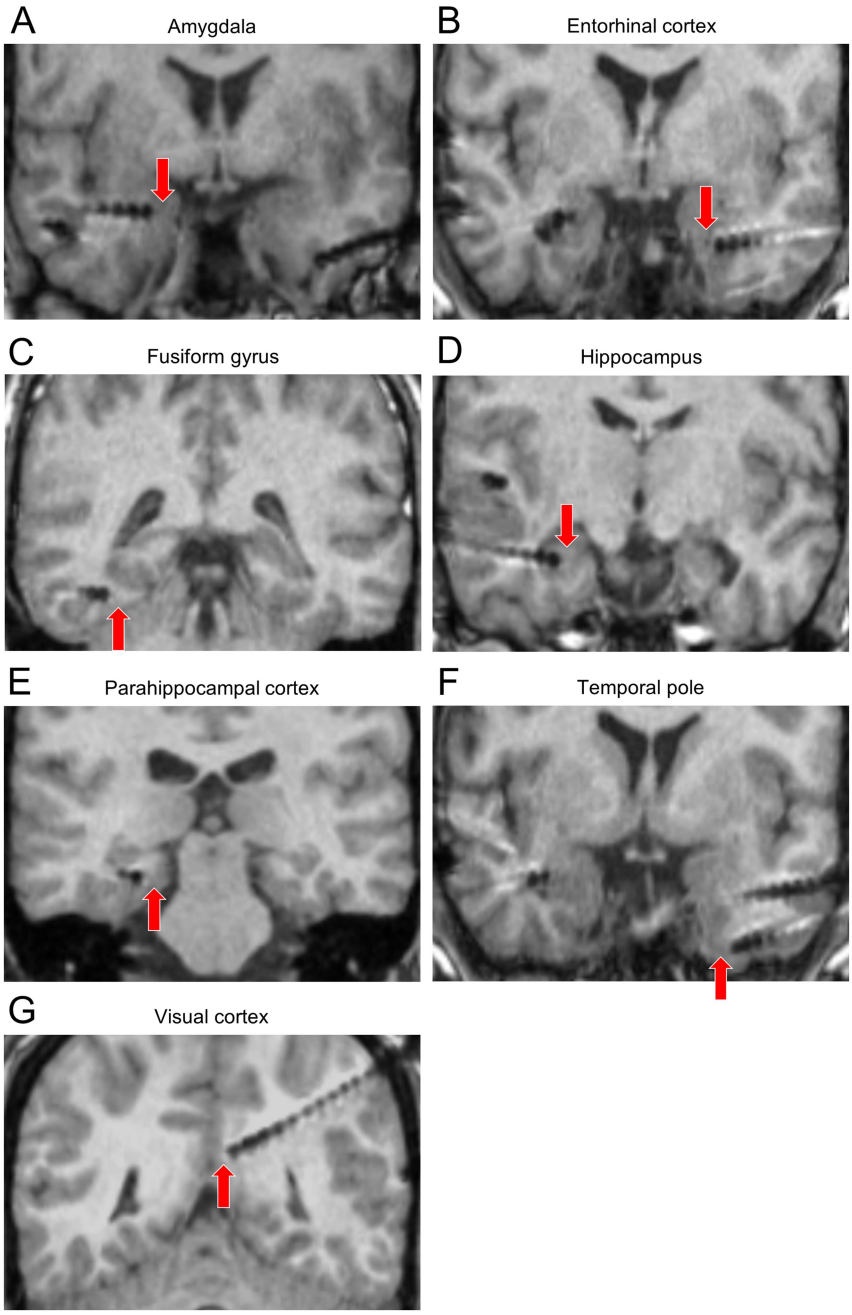

Fig. S1. Examples of microelectrode locations. (**A-G**) Example microelectrode locations in amygdala, entorhinal cortex, fusiform gyrus, hippocampus, parahippocampal cortex, temporal pole, and visual cortex. Electrode contacts of depth electrodes appear as dark circles on the MRI scans. Red arrows point at putative microelectrode locations, which protrude 3-5 mm from the tip of the depth electrode (often not visible on MRI scans).

bioRxiv preprint doi: https://doi.org/10.1101/2020.03.03.973131; this version posted March 31, 2020. The copyright holder for this preprint (which was not certified by peer review) is the author/funder, who has granted bioRxiv a license to display the preprint in perpetuity. It is made available under aCC-BY-NC-ND 4.0 International license.

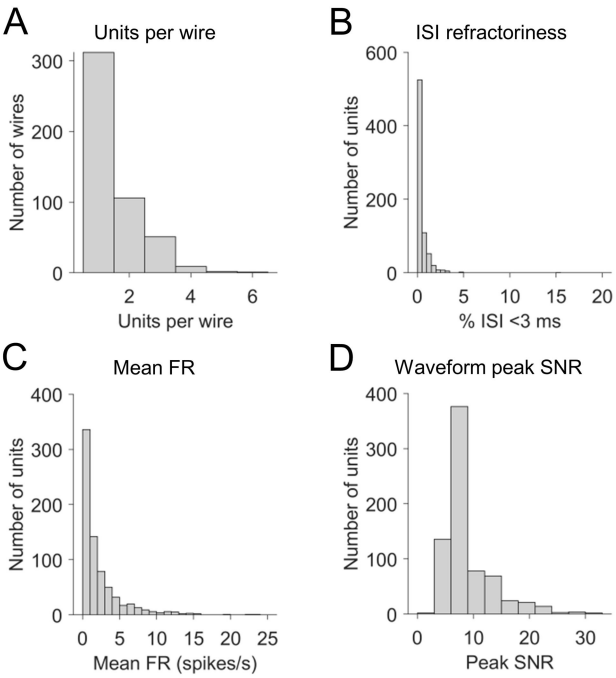

Fig. S2. Quality assessment of neuronal recordings. (**A**) Histogram of units per wire. On average, 1.516 ± 0.037 units per wire (mean ± SEM) were recorded. (**B**) Histogram of the percentages of inter-spike intervals (ISIs) that were shorter than 3 ms. On average, units exhibited 0.434 ± 0.031% ISIs that were shorter than 3 ms (mean ± SEM). All units except for one had a value of <5%. (**C**) Histogram of mean firing rates (FRs). On average, units exhibited mean FRs of 2.268 ± 0.112 spikes/s (mean ± SEM). (**D**) Histogram of the mean waveform peak signal-to-noise ratio (SNR) of each unit. On average, the SNR of the mean waveform peak was 8.820 ± 0.168 (mean ± SEM), similar to previous reports [e.g., (*51*)].

bioRxiv preprint doi: https://doi.org/10.1101/2020.03.03.973131; this version posted March 31, 2020. The copyright holder for this preprint (which was not certified by peer review) is the author/funder, who has granted bioRxiv a license to display the preprint in perpetuity. It is made available under aCC-BY-NC-ND 4.0 International license.

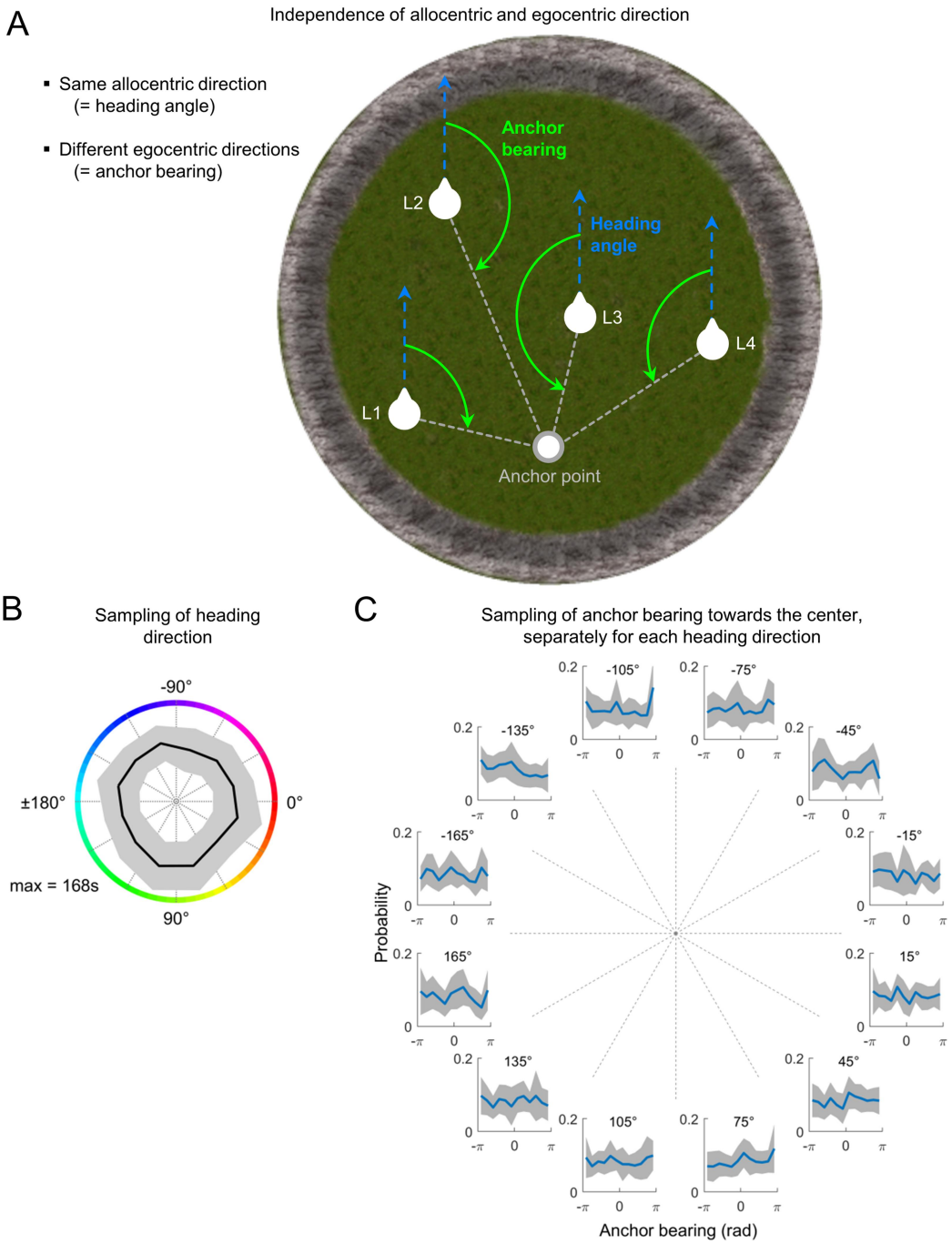

770 **Fig. S3. Sampling of egocentric and allocentric direction.** (**A**) In allocentric coordinates, directional information is determined relative to the external world (for example, a specific location can be "south"). In egocentric coordinates, directional information is determined in relation to the self (for example, a specific location can be to the right of the subject). This diagram illustrates the general independence of egocentric anchor bearing and allocentric
775 heading direction. A potential anchor point is depicted in the south part of the environment (gray circle). At different locations within the virtual environment (L1 to L4), the allocentric heading angle of the navigating subject is identical (light blue, dashed arrows), but the egocentric anchor bearings are different (light green arrows). White dashed lines, vectors between the subject's locations and the anchor point. (**B**) Sampling of allocentric heading
780 direction. Black line, mean across patients; gray area, STD across patients; max, maximum of

bioRxiv preprint doi: https://doi.org/10.1101/2020.03.03.973131; this version posted March 31, 2020. The copyright holder for this preprint (which was not certified by peer review) is the author/funder, who has granted bioRxiv a license to display the preprint in perpetuity. It is made available under aCC-BY-NC-ND 4.0 International license.

direction-specific mean dwell times. (**C**) For each allocentric heading direction, the distribution of egocentric anchor bearings towards the environmental center is depicted, which is chosen as an example anchor point. Distributions are expressed as probabilities. A bearing of 0 corresponds to "anchor point ahead" and ±π corresponds to "anchor point behind". Negative bearing values correspond to "anchor point to the left". Blue line, mean across patients; gray area, STD across patients. Numbers above each subpanel indicate the allocentric heading direction for which the distribution of bearings is shown (with negative allocentric heading directions pointing north).

bioRxiv preprint doi: https://doi.org/10.1101/2020.03.03.973131; this version posted March 31, 2020. The copyright holder for this preprint (which was not certified by peer review) is the author/funder, who has granted bioRxiv a license to display the preprint in perpetuity. It is made available under aCC-BY-NC-ND 4.0 International license.

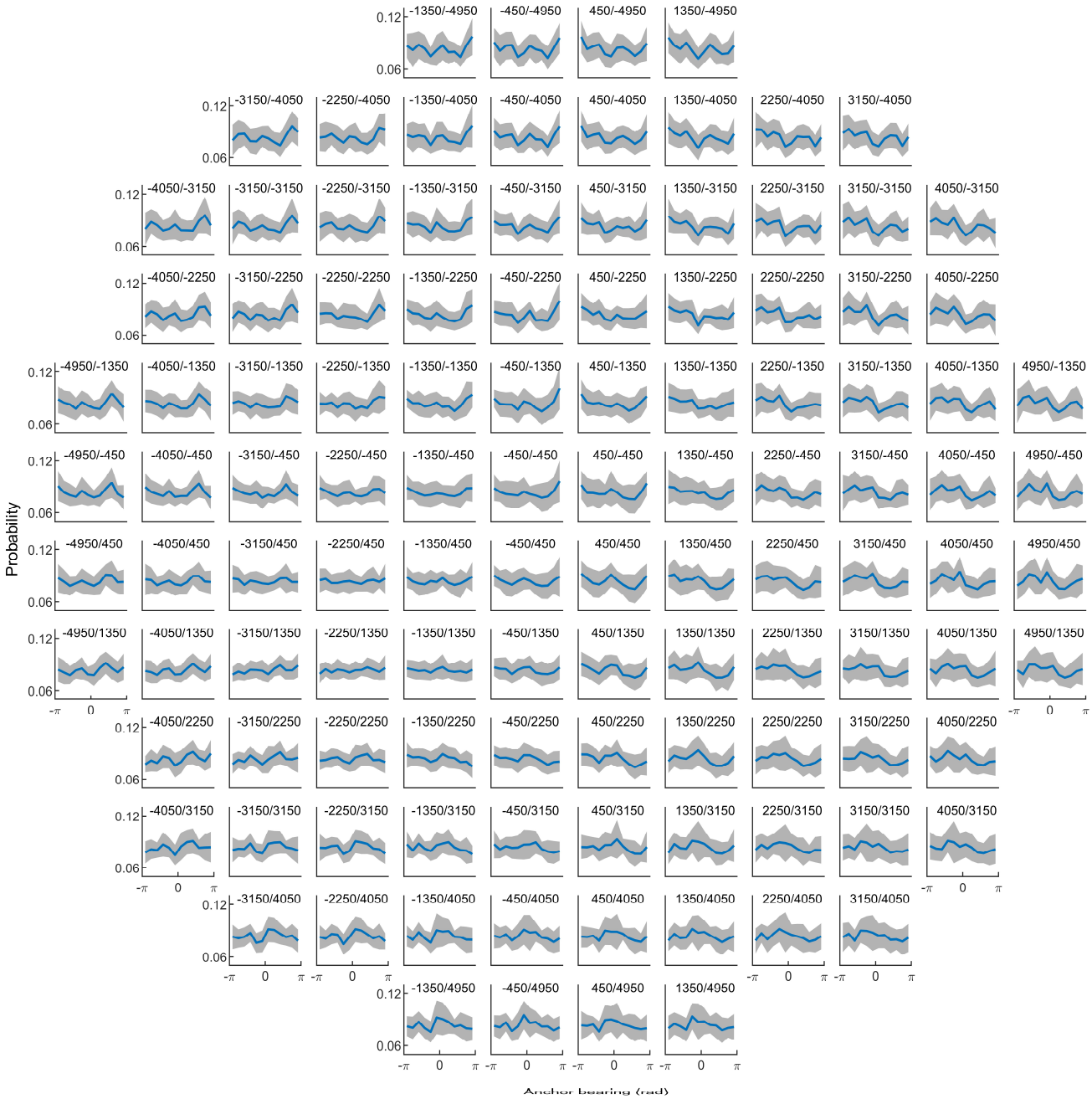

790 **Fig. S4. Sampling of egocentric bearing towards candidate anchor points.** For each candidate anchor point, the distribution of bearings towards this candidate point is depicted. Distributions are expressed as probabilities. An anchor bearing of 0 corresponds to "anchor point ahead" and ±π corresponds to "anchor point behind". Negative values correspond to "anchor point to the left". Blue line, mean across patients. Gray area, STD across subjects.
795 Numbers above each subpanel indicate the (x/y)-coordinate of the candidate anchor point (candidate points with negative y-values are located in the "north" part of the environment).

bioRxiv preprint doi: https://doi.org/10.1101/2020.03.03.973131; this version posted March 31, 2020. The copyright holder for this preprint (which was not certified by peer review) is the author/funder, who has granted bioRxiv a license to display the preprint in perpetuity. It is made available under aCC-BY-NC-ND 4.0 International license.

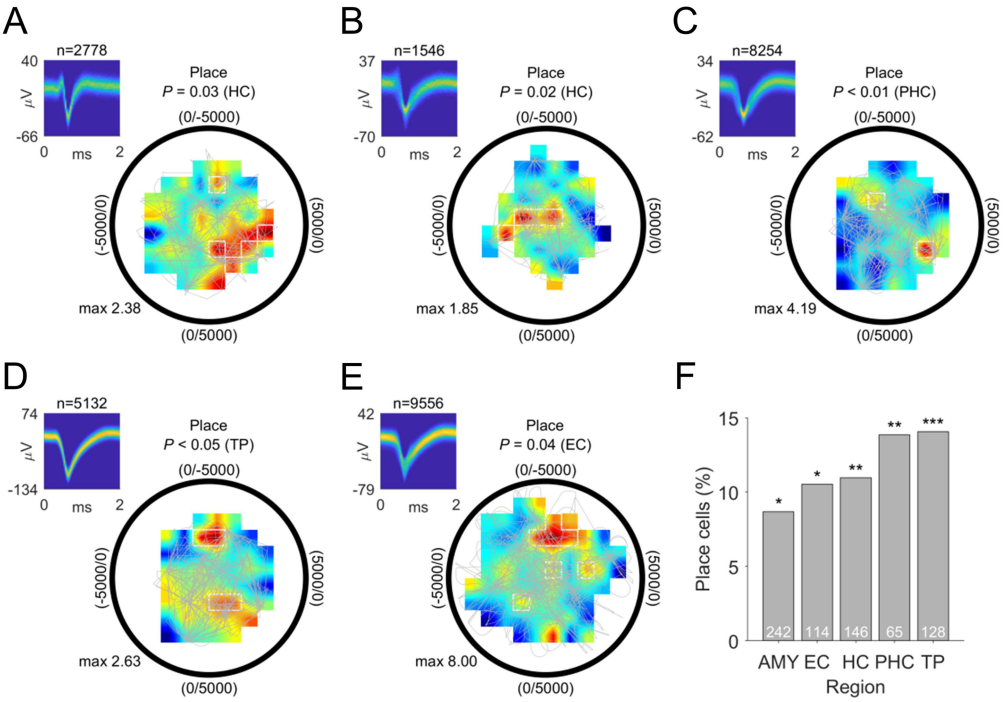

Fig. S5. Place cells. (**A-E**) Examples of place cells. The hippocampal place cell shown in (**A**) increased its firing rate whenever the subject was in the southeast part of the environment. Colored areas depict smoothed firing rates as a function of place (dark blue, low firing rate; dark red, high firing rate); max, maximum firing rate (Hz). White line delineates place bins. Gray line, patient's navigation path. Only bins with ≥5 separate traversals were included in the analysis to ensure sufficient behavioral sampling. Black circle, environmental boundary. Upper left subpanels show spike-density plots (number above subpanel indicates spike number entering the analysis); ms, milliseconds. (**F**) Distribution of place cells across brain regions (n=84; binomial test, P<0.001). AMY, amygdala; EC, entorhinal cortex; HC, hippocampus; PHC, parahippocampal cortex; TP, temporal pole. *P<0.05; **P<0.01; ***P<0.001.

bioRxiv preprint doi: https://doi.org/10.1101/2020.03.03.973131; this version posted March 31, 2020. The copyright holder for this preprint (which was not certified by peer review) is the author/funder, who has granted bioRxiv a license to display the preprint in perpetuity. It is made available under aCC-BY-NC-ND 4.0 International license.

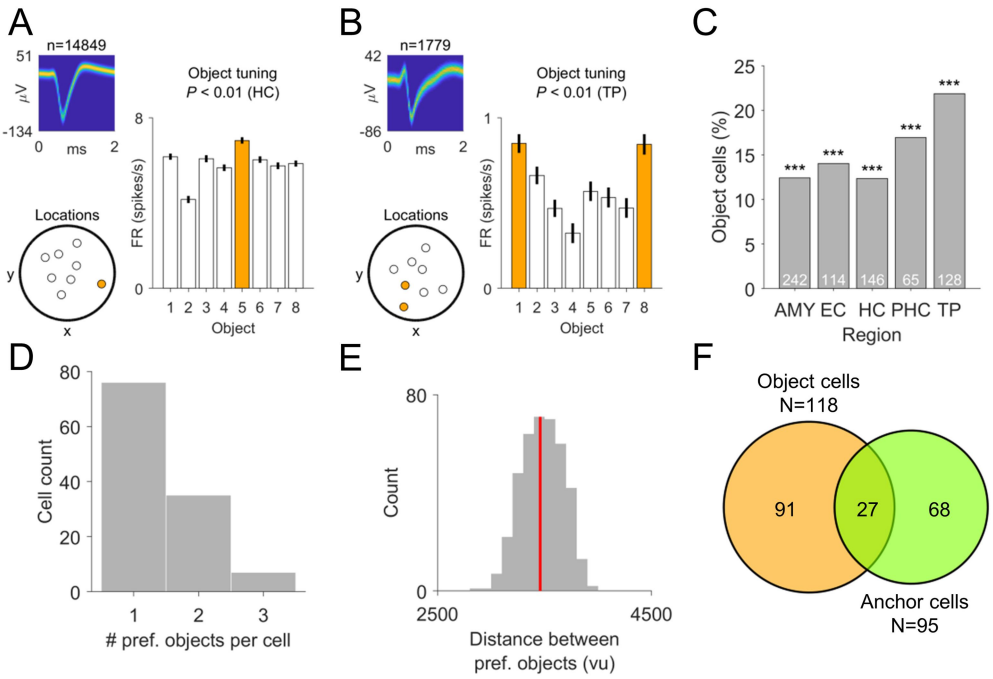

Fig. S6. Object cells. (**A-B**) Examples of object cells. Each bar shows the average firing rate (FR) during trials with a given object. Orange bars depict the cells' preferred object(s), which we defined as those objects that were associated with firing rates above the 95th percentile of surrogate firing rates. For example, the object cell shown in (**A**) activated during trials in which object #5 (in this case, the globe) had to be retrieved and re-encoded. Error bars indicate SEM. Upper left subpanels show spike-density plots (number above subpanel indicates spike count entering the analysis). Lower left subpanels show the object locations (locations of preferred objects are indicated in orange). (**C**) Distribution of object cells across brain regions. (**D**) Histogram of the number of preferred ("pref.") objects per object cell. (**E**) When object cells exhibited more than one preferred ("pref.") object, the locations of the preferred objects were not spatially closer to each other as compared to similar numbers of randomly selected object locations (permutation test, P=0.464), suggesting that object cells represented objects in a way that was not mainly determined by information about the associated spatial locations of the objects. Red line, empirical average distance between preferred objects; gray bars, histogram of surrogate distances. (**F**) Overlap between object cells and anchor cells. AMY, amygdala; EC, entorhinal cortex; HC, hippocampus; PHC, parahippocampal cortex; TP, temporal pole. ***P<0.001.

bioRxiv preprint doi: https://doi.org/10.1101/2020.03.03.973131; this version posted March 31, 2020. The copyright holder for this preprint (which was not certified by peer review) is the author/funder, who has granted bioRxiv a license to display the preprint in perpetuity. It is made available under aCC-BY-NC-ND 4.0 International license.

Supplementary Tables

Table S1. Patients.

Patient	Sessions	Total number of trials
Freiburg_001	Freiburg_001a	39
	Freiburg_001b	78
Freiburg_002	Freiburg_002	34
Freiburg_003	Freiburg_003a	167
	Freiburg_003b	162
Freiburg_004	Freiburg_004a	166
	Freiburg_004b	162
Freiburg_005	Freiburg_005	54
Freiburg_006	Freiburg_006	98
Freiburg_007	Freiburg_007	36
Freiburg_008	Freiburg_008	67
Freiburg_009	Freiburg_009	162
Freiburg_010	Freiburg_010	102
Freiburg_011	Freiburg_011	54
Freiburg_012	Freiburg_012	102
Freiburg_013	Freiburg_013a	167
	Freiburg_013b	164
Freiburg_014	Freiburg_014	94